Chemistry Europe
European Chemical Societies Publishing

WILEY VCH

Excellence in Chemistry Research

Announcing our new flagship journal

- Gold Open Access
- Publishing charges waived
- Preprints welcome
- Edited by active scientists

Meet the Editors of *ChemistryEurope*

Luisa De Cola
Università degli Studi di Milano Statale, Italy

Ive Hermans
University of Wisconsin-Madison, USA

Ken Tanaka
Tokyo Institute of Technology, Japan

Batteries & Supercaps

Research Article
doi.org/10.1002/batt.202300308

Chemistry Europe
European Chemical Societies Publishing

www.batteries-supercaps.org

VIP *Very Important Paper*

Special Collection

A π-Conjugated Porphyrin Complex as Cathode Material Allows Fast and Stable Energy Storage in Calcium Batteries

Thomas Smok,[a, b] Shirin Shakouri,[b] Ebrahim Abouzari-Lotf,[a, b] Frank Pammer,[a] Thomas Diemant,[a] Saibal Jana,[b] Ananyo Roy,[a] Yanlei Xiu,[a] Svetlana Klyatskaya,[b] Mario Ruben,*[b, c, d] Zhirong Zhao-Karger,[a, b] and Maximilian Fichtner*[a, b]

Rechargeable calcium batteries (RCB) are prospective candidates for sustainable energy storage, as they hold the promise of the high energy density of lithium-ion batteries (LIBs) while simultaneously combining it with highly abundant raw materials. However, for long time, calcium batteries have faced severe issues with regard to cycling stability, until recently developments demonstrated improved battery cycle life when employing CaSn alloy anodes with fluorinated alkoxyborate electrolytes. These findings opened up the possibility to study cathode materials for RCBs not only in a more comparable manner, but also in a practical full cell design. As representative of emerging organic electrode materials (OEMs), we investigated tetrakis(4-pyridyl) porphyrin as both free ligand (H_2TPyP) and in the form of its copper MOF complex (CuTPyP–MOF) as active cathode species in RCBs. The cells demonstrated high capacities and excellent cycling stability at the same time. Even at elevated current densities of e.g., 2000 mA/g the full cells delivered stable capacities of ~90 mAh/g proving its excellent rate capability. This study explores the electrochemical performance of porphyrin active materials in calcium batteries and represents a significant step forward in the progress toward organic electrodes for multivalent energy storage systems.

Introduction

With the continuous electrification of societies due to the growing usage of portable consumer electronics and electric vehicles, the demand for energy storage has been constantly increasing.[1] So far, lithium-ion batteries (LIBs) are leading the world market for secondary batteries as the currently best solution for reliable electrochemical energy storage.[2] However, LIBs have nearly reached their theoretical limits in terms of energy density and are still lacking high-level of safe storage mechanisms.[3] Moreover, given the limited availability of certain raw materials (e.g., Li, Co, Ni),[4] a shift towards more economic, and at the same time sustainable, cell chemistries is highly desired.[5] A common approach to address the aforementioned issues is the use of highly abundant materials based on multivalent elements like Mg, Ca or Al.[5b,6] Multivalent batteries might become an alternative to LIBs as they hold the possibility of higher energy densities due to transferring two or more charges per carrier ion.[7,8] Also, dendrite formation seems to be less significant in these types of storage systems.[9]

The rechargeable calcium battery (RCBs) is an emerging multivalent system, that is poised to exhibit high energy densities due to the inherently low reduction potential (−2.87 V vs. SHE)[5a,10] of calcium.[5a,10] Calcium is significantly more abundant in the earth's crust in comparison with other elements like Li, Na, K, Zn and Mg.[11] As a result, the production costs for RCBs could be lower, making them a more economic option for energy storage.[11,12] Compared to their homologous Mg^{2+} ions (ion radius 0.86 Å, charge density $\rho = 120$ C mm^{-3}, coordination number 6),[13] Ca^{2+} ions (ion radius 1.14 Å, charge density $\rho = 52$ C mm^{-3}, coordination number 6)[13] are relatively large in size.[14] This allows the charge to be distributed over a larger volume, resulting in "softer ions".[10] The softness of Ca ions provides two key advantages. First, it reduces the energy barrier of the de-solvation of Ca ions making cycling more straightforward and stable. Second, the lowered charge density of the bare ion results in energetically more favorable solid-

[a] T. Smok, Dr. E. Abouzari-Lotf, Dr. F. Pammer, Dr. T. Diemant, A. Roy, Dr. Y. Xiu, Dr. Z. Zhao-Karger, Prof. Dr. M. Fichtner
Helmholtz Institute Ulm (HIU) Electrochemical Energy Storage
Helmholtzstraße 11, 89081 Ulm (Germany)
E-mail: m.fichtner@kit.edu

[b] T. Smok, S. Shakouri, Dr. E. Abouzari-Lotf, Dr. S. Jana, Dr. S. Klyatskaya, Prof. Dr. M. Ruben, Dr. Z. Zhao-Karger, Prof. Dr. M. Fichtner
Institute of Nanotechnology, Karlsruhe Institute of Technology
Hermann-von-Helmholtz-Platz 1, 76344 Eggenstein-Leopoldshafen (Germany)
E-mail: mario.ruben@kit.edu

[c] Prof. Dr. M. Ruben
Institute of Quantum Materials and Technologies (IQMT)
Karlsruhe Institute of Technology
Hermann-von-Helmholtz-Platz 1, 76344 Eggenstein-Leopoldshafen (Germany)

[d] Prof. Dr. M. Ruben
Centre Européen de Science Quantique (CESQ)
Institut de Science et d'Ingénierie Supramoléculaires (ISIS, UMR 7006)
CNRS-Université de Strasbourg
8 allée Gaspard Monge BP 70028 67083, Strasbourg Cedex (France)

Supporting information for this article is available on the WWW under https://doi.org/10.1002/batt.202300308

This publication is part of a joint Special Collection dedicated to Post-Lithium Storage, featuring contributions published in Advanced Energy Materials, Batteries & Supercaps, and ChemSusChem.

Research Article
doi.org/10.1002/batt.202300308
Chemistry Europe
European Chemical Societies Publishing

state diffusion within the electrodes.[15] This leads to enhanced cycling kinetics and higher power densities.

Despite these inherent advantages of RCBs, their development is still hindered by several challenges that need to be overcome.[16] One of the main obstacles is the severe passivation of metal anodes, leading to low cycling stability.[17] The lack of available ambient temperature electrolytes for RCBs also led to a stagnation of progress in this field of research.[18] However, recent studies have shown that these issues can be diminished by using CaSn-alloys as anodes in combination with calcium tetrakis-(hexafluoroisopropyloxy)-borate ($Ca[B(hfip)_4]_2$) electrolytes.[19] In consequence, the so increased stability of the anodes allowed for testing in a realistic full-cell design. With the now improved cell design, stable cycling behavior of up to 5000 cycles was observed, proving enhanced Ca stripping/plating efficiency of the alloy compared to metallic calcium anodes.[19a] These findings have opened up novel pathways for testing other potential cathode materials without requiring impractical cell designs like, e.g., the use of carbon electrodes.[20]

Compared to inorganics electrode materials with sluggish reaction kinetics,[21] organic electrode materials (OEMs) are often employed as cathodes of multivalent systems, because they show less rigid migration pathways for ions and lowered migration barriers due to their less dense structures.[22] OEMs offer nearly limitless structural varieties paired with tunable functionalities[23] making them excellent candidates to fulfill the requirements for complicated multivalent batteries, such as hosting larger and stronger polarizing ions.[24] Among the potential organic compounds, porphyrins represent a promising class of OEMs that have been successfully utilized in various cell chemistries with both mono- and multivalent ions, including Li-,[25] Na-,[26] K-,[27] Al-[28] and Mg-[29] based storage systems. Porphyrins are known for their ability to rapidly take up and release multiple electrons (Figure 1a).[30] This ambipolar behavior, also known as *b-type* material, enables high specific capacities (compared to *p-type* materials) and high voltage (compared to *n-type* materials), resulting in high energy densities comparable to commercial inorganic compounds.[25,31] Additionally, recent publications have shown that porphyrin materials can efficiently insert and de-insert multivalent ions at high cycling rates, what enables high rate performances and power densities in i.e. rechargeable magnesium batteries (RMBs).[29] Inspired by the remarkable performances of porphyrinoids as cathode materials, we report here for the first time on the electrochemical behavior of 5,10,15,20-tetra(4-pyridyl)-porphyrin (H_2TPyP) and a H_2TPyP-based copper metal organic framework (CuTPyP–MOF) in calcium batteries. These materials were utilized as cathodes against calcium tin alloys in a borated electrolyte (Figure 1b) in the follow up of our previous work.[19a]

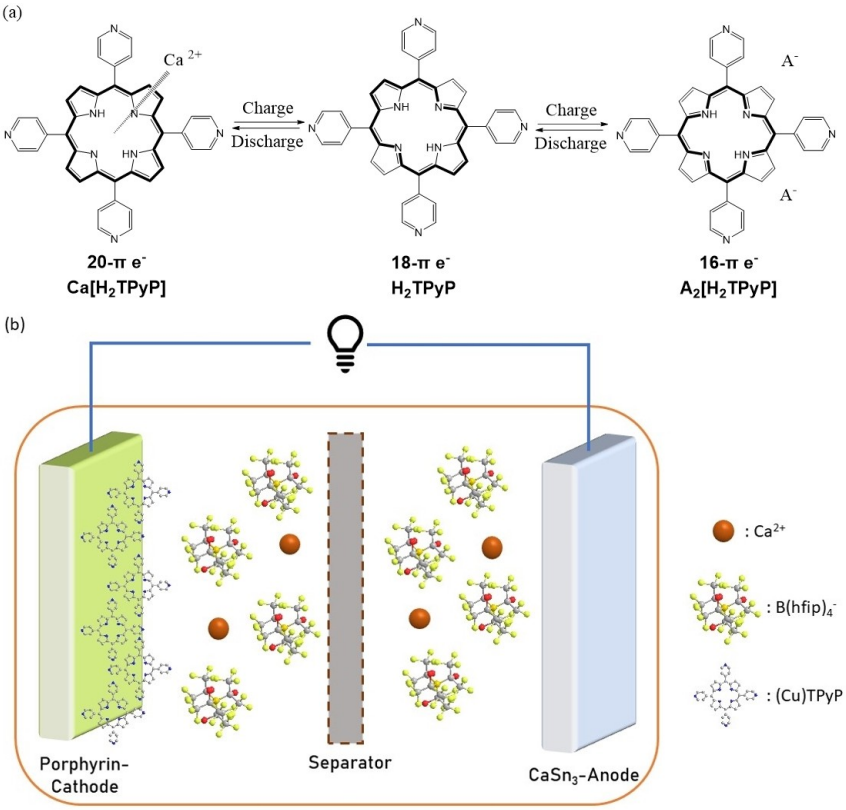

Figure 1. A general description of a) the charge storage mechanism of tetra pyridyl porphyrins in calcium batteries, where the delocalized redox sites allow their utilization in the calcium cells presented in b).

Research Article
doi.org/10.1002/batt.202300308
Chemistry Europe
European Chemical Societies Publishing

Results and Discussion

5,10,15,20-tetra(4-pyridyl)-porphyrin (H_2TPyP), a commercially available porphyrin, was used in a one pot reaction for complexation with Cu(II) (Figure S1). While some literature describes the reaction to result in a single Cu porphyrin complex,[32] our experiment led to the formation of a porphyrin-based metal-organic framework (MOF) connected via dicopper(II) tetraacetate clusters ($Cu_2(OAc)_4$) as linker molecules. The structure is already known in literature and well described by single-crystal X-ray crystallography.[33] Surprisingly, the described synthesis of the MOF[33b,34] is similar to the one for single porphyrin molecule.[32b] A first strong indicator for the formed MOF structure was given by elemental analysis (Table S1), showing much lower carbon proportions than for the isolated, non-connected porphyrin complex expected. Based on theoretical calculations and experimental elemental analysis, we propose the presence of $CuTPyP \cdot (Cu_2(OAc)_4)_2$, wherein two dicopper(II) tetraacetate clusters (paddlewheel cluster) are coordinated to one of the four pyridyl functionalities. This constitutes the smallest building unit of the 2-D coordination network.[34] Further analysis by infrared spectroscopy verified the presence of acetate functional groups (Figure S2), corroborating their function as linking unit. The strong peaks at 1619, 1603 and 1422 cm^{-1} correspond to asymmetric and symmetric carboxylate ($-CO_2^-$) stretching vibrations.[35]

The formation of MOF-structures was further studied by XPS measurements, which showed a significant amount of Cu(I) already in the pristine state (Figure 2a). Such ions would be very uncommon and improbable for mono-molecular porphyrins, where only the conjugated porphyrin macrocycle is complexed by a copper ion. Previous research on Cu–MOFs reported that especially at the nodes of MOF structures, copper show the oxidation state +1.[36] Therefore, we speculate that the Cu(I)-formation observed in our study might originate from active unsaturated metal sites (UMS) within the copper-based MOFs.[36] Also further possibilities, like defects[37] in the MOF structure or Cu_2O impurities[38] are possible and should be considered. These defects may for example explain the reduced amount of nitrogen found in elemental analysis.

To confirm the crystallinity of the synthesized material and compare it with literature,[33b] powder X-ray diffraction patterns were recorded (Figure 2b, red line). Despite matching reflexes in the pattern, the prepared sample exhibits lower crystallinity than literature,[33b] which can be attributed to two factors. Firstly, the faster crystallization process employed in this study may contribute to reduced crystallinity. Secondly, the presence of solvent molecules encapsulated within the material, which can be lost during the drying process, is supposed to affect the crystalline structure of the sample. This phenomenon is illustrated by the comparison of as-prepared and dried MOF samples (Figure S3). The release of trapped solvent molecules

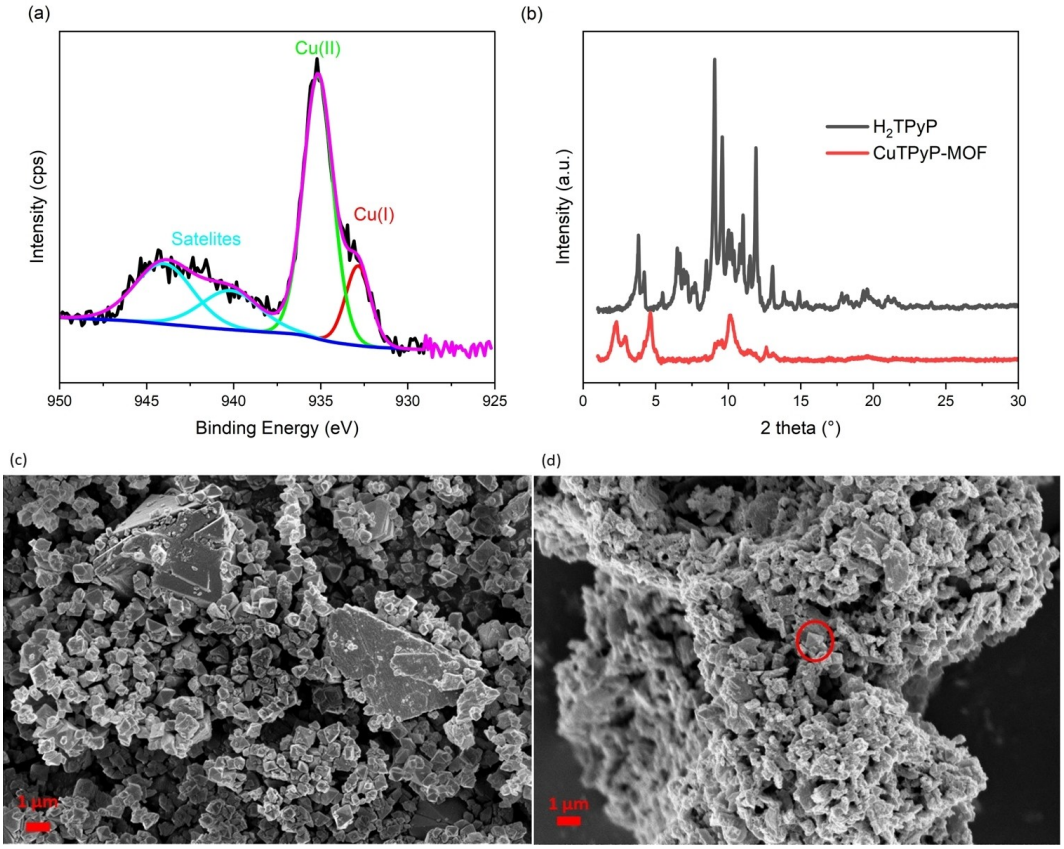

Figure 2. a) XPS $Cu2p_{3/2}$ detail spectrum of CuTPyP–MOF. b) XRD shows a high crystallinity of copper-free porphyrin, which can also be observed in c) SEM images of H_2TPyP. d) In contrast, CuTPyP–MOF is less crystalline, however, it still consists of polygonal crystallites (red circle).

induces the closed-open transition, which is a crucial characteristic of these materials resulting in the lowered total crystallinity.[39]

In good agreement to the XRD results, also the SEM images show a similar reduction of crystallinity when examining CuTPyP–MOF. While the samples made from the precursor ligand H_2TPyP (Figure 2c) consist of regularly shaped, single polygonal particles with a smooth surface, rather larger agglomerated structures are present in CuTPyP–MOF (Figure 2d). These structures, however, consist of single polygonal particles (red circle) which might indicate that a part of the original appearance was kept. In accordance with this, the particle size of both materials does not differ essentially, as it is for both materials around 1 μm. Therefore, we do not expect an influence of the particle size when comparing the electrochemical properties of these materials.

A common problem of porphyrins as well as other organic materials that impacts the electrochemical performance is the high solubility of active compounds in the electrolytes.[40] In earlier studies it was already found that introducing metal atoms into the porphyrin structure might be beneficial for closing the solubility gap.[25a,41] Also, in the case of H_2TPyP, which has an inherently low solubility, the dissolution in DME was further reduced after copper complexation (Figures S4 and S5). Although already minor dissolved traces will lead to a color change, even after several days the vast amount stays undissolved. When incorporating Cu into the porphyrin core an increase in symmetry of the molecule is achieved which becomes visible by the loss of two Q-bands in the UV-Vis spectrum (Figure S6b). The redshift, derived from the same spectrum, can be explained by computational calculations using density functional theory (DFT). Therefore, improved understanding of the origin of the redshift of the Q-band in UV spectra after Cu(II) insertion was gained by performing time-dependent DFT (TDDFT) calculations with the goal to find the electronic transitions and relationships between occupied and unoccupied molecular orbitals. In the ligand H_2TPyP, based on the oscillator strength (*f*), the first weak transition at 562 nm gave rise to the typical Q-band. This transition mainly originates from the combined interactions of four orbitals (HOMO→LUMO, 60%; HOMO-1→LUMO + 1, 40%). Contrarily, in the case of single molecule CuTPyP, the Q-band emerges at 576 nm due to the electronic transition with the main contribution from SOMO-1→LUMO + 1 (96%) (Figure S7).

H_2TPyP and the isolated molecular complex CuTPyP were further studied by DFT. The correlation between the two compounds serves to estimate the electronic effect of the pyridyl-substituent and its possible impact on redox processes. The peripheral 4-pyridyl-substitutents in H_2TPyP-systems stand at dihedral angles of ca. 70° relative to the plane of the porphyrin ring. This limits the effective conjugation between the macrocyclic ring system and the substituents. Accordingly, the free base shows virtually no involvement of the substituents between the highest occupied orbital-1 (HOMO-1) and the lowest unoccupied orbital + 1 (LUMO + 1) in the frontier orbital plots (Figure S7).

Introduction of the central copper atom alters the electronic structure, with the d^9-configuration of the central atom resulting in a doublet spin state. Nonetheless, introduction of Cu (II) in CuTPyP leaves the energy level of the HOMOs virtually unchanged (H_2TPyP: HOMO = -5.61 eV, CuTPyP; SOMOs-α = −5.61, β = 5.64 eV). The central atom contributes only marginally to the frontier orbitals SOMO-1 through LUMO, which are π-orbitals very similar to those in the free ligands.

To obtain more insights into the electrochemical processes occurring during initial cycling, cyclic voltammetry experiments with a sweep rate of 1 mV/s were performed. In both porphyrin materials the insertion of calcium ions can be observed, which occurs roughly at 0.7 V for H_2TPyP and at 0.8 V for CuTPyP–MOF during the discharge. The deinsertion process during the charging step occurs at a potential of 1.1 V for H_2TPyP and 0.9 V for CuTPyP–MOF (Figure 3a, b). Interestingly, for H_2TPyP the reduction peak intensity is much larger and strongly reduces in the consecutive cycles assuming that a part of calcium ions is irreversibly trapped inside the electrode. The corresponding charge discharge profiles of galvanostatic cycling (Figure 3c) show for H_2TPyP a similar feature by the formation of a large plateau during discharge in the region of 0.7 V.

As the porphyrin core is known to readily host metal ions, we assume that calcium ions are bonded within the central cavity of porphyrins of H_2TPyP during the discharge process. Computational results indicate that, structural reorientation of H_2TPyP and CuTPyP occurs during Ca ion insertion and deinsertion. In the case of H_2TPyP, the central coordination site provides ample space for strong interaction with the Ca ion resulting in a computed deinsertion energy of 3.95 eV/mol. However, due to the strong interactions, reversibility is significantly diminished, and further irreversible reactions may occur with low probability, given that the reaction energy is positive (0.66 eV/mol). In contrast, CuTPyP does not allow for direct Ca ion insertion, as the central position is already occupied by copper ion. To enable Ca ion insertion, the copper ion must be displaced from the central cavity (Figure S8). This displacement lowers the deinsertion energy of CuTPyP by 1.27 eV/mol (the deinsertion energy of a single molecule CuTPyP is 2.68 eV/mol), making deinsertion more likely and efficient during charging. However complete removal of copper from the central cavity and insertion of Ca ions or partial reduction of the central copper are highly improbable due to their positive reaction energies, measuring 2.03 eV/mol and 2.94 eV/mol, respectively (Scheme S1).

This (de)insertion process significantly impacts calcium storage in H_2TPyP and therefore influences the discharge capacity of the battery (Figure 3c). While H_2TPyP initially achieves a high discharge capacity of 176 mAh/g, this value drops rapidly down to 135 mAh/g in the second cycle. The CuTPyP–MOF offers an advantage in terms of better reversibility of calcium insertion/deinsertion, which can be observed in the following cycles, where capacities up to 162 mAh/g are achieved (Figure 3d). Notably, the achieved capacities are in both cases (H_2TPyP and CuTPyP–MOF) above theoretical values for a two-electron transfer. Therefore, we speculate on a partial contribution coming from anion-storage as presented earlier

Research Article
doi.org/10.1002/batt.202300308
Chemistry Europe
European Chemical Societies Publishing

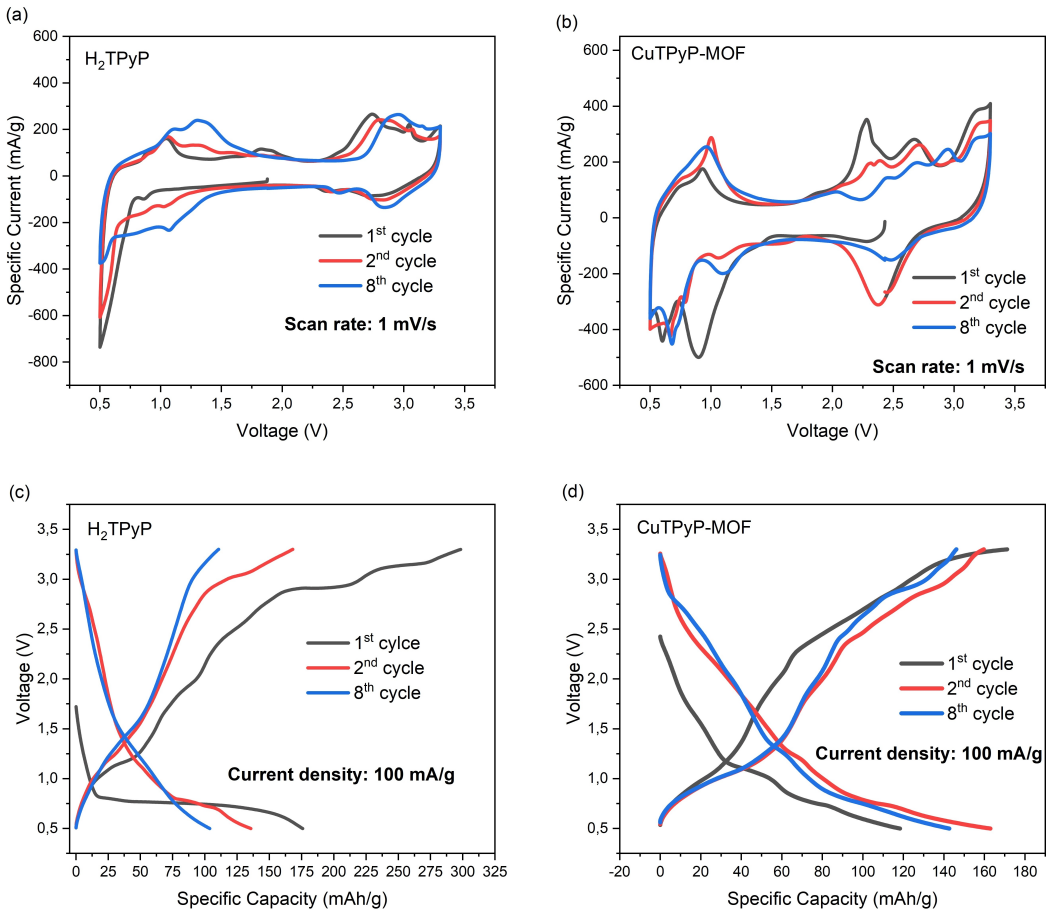

Figure 3. Cyclic voltammograms of a) H_2TPyP (a) and b) CuTPyP–MOF in the range of 0.5 to 3.3 V measured with a scan rate of 1 mV/s. The corresponding charge-discharge profiles of c) H_2TPyP and d) CuTPyP–MOF cycled with a current density of 100 mA/g.

(Figure 1a). This consideration is supported by XPS-data in C1s and B1s regions (Figures S9 and S10) which show effective presence of the anion by occurrence of CF_x- and B- functionalities in the cycled electrodes. The corresponding mechanism is already known and was discussed in literature before.[32a]

The calcium ion insertion mechanism was further studied by means of *ex-situ* XPS measurements. Detail measurements in the Ca 2p region from electrodes in pristine, charged and discharged state are shown in Figure 4; while the results of measurements in other regions are compiled in Figures S9 and S10 for H_2TPyP and CuTPyP–MOF, respectively. The results in Figure 4 confirm the presence of calcium ions in the cycled electrodes. As expected, the percentage of calcium ions in the discharged electrodes was higher than in the charged ones, demonstrating the insertion during discharge. Based on quantitative analysis of the XPS detail spectra, calcium percentages in the surface layer of the charged and discharged electrodes of H_2TPyP were 0.58% and 1.91%, respectively, while for CuTPyP–MOF, the percentages were 0.16% and 3.68% respectively. The results are in excellent agreement with SEM-EDX measurements (Figures S11–S19), which showed a uniform distribution of calcium for both materials. Furthermore, the Ca/Cu ratio [2.33 in the discharged versus 0.3 in the charged state] obtained by SEM-EDX showed a similar trend for the calcium insertion in CuTPyP–MOF. This clearly points out that calcium ions are inserted into the electrodes during the discharge and supports earlier discussed ion-trapping during charge.

In the CuTPyP–MOF-system, a reversible redox reaction of the copper central metal atom is taking place. A comparative CV measurement (Figure S20) suggests that an additional redox peak, which occurs at 2.7 V in the anodic scan and reverses at 2.5 V in the cathodic scan, could be attributed to the copper atom in the porphyrin core structure. Previous research also reported on partial Cu(II) to Cu(I) redox reaction in Cu–porphyrins.[25a,29,41a,42] However, in this study, we observe the reaction to be more reversible and complete than previous studies have suggested. Based on *ex-situ* XPS measurements (Figure 5) of the Cu 2p region, a significant formation of Cu(I) in the fully discharged state could be shown. During discharge, the injection of additional electrons in the d-orbital leads to the reduction of Cu(II) to Cu(I), as the electrochemical reduction is expected to fundamentally alter the electronic structure of the material. Computed structures of the singlet mono-anion $[CuTPyP]^{-1}$ (Figure S21) show the HOMO to be a non-bonding orbital that is exclusively delocalized across the Cu-centered dx^2-y^2-orbital[43] and the Cu–pyrrolo-σ bonds. In the neutral complex CuTPyP, the spin density is delocalized throughout the same area, i.e., the dx^2-y^2-orbital (Figure S22).

Research Article
doi.org/10.1002/batt.202300308
Chemistry Europe
European Chemical Societies Publishing

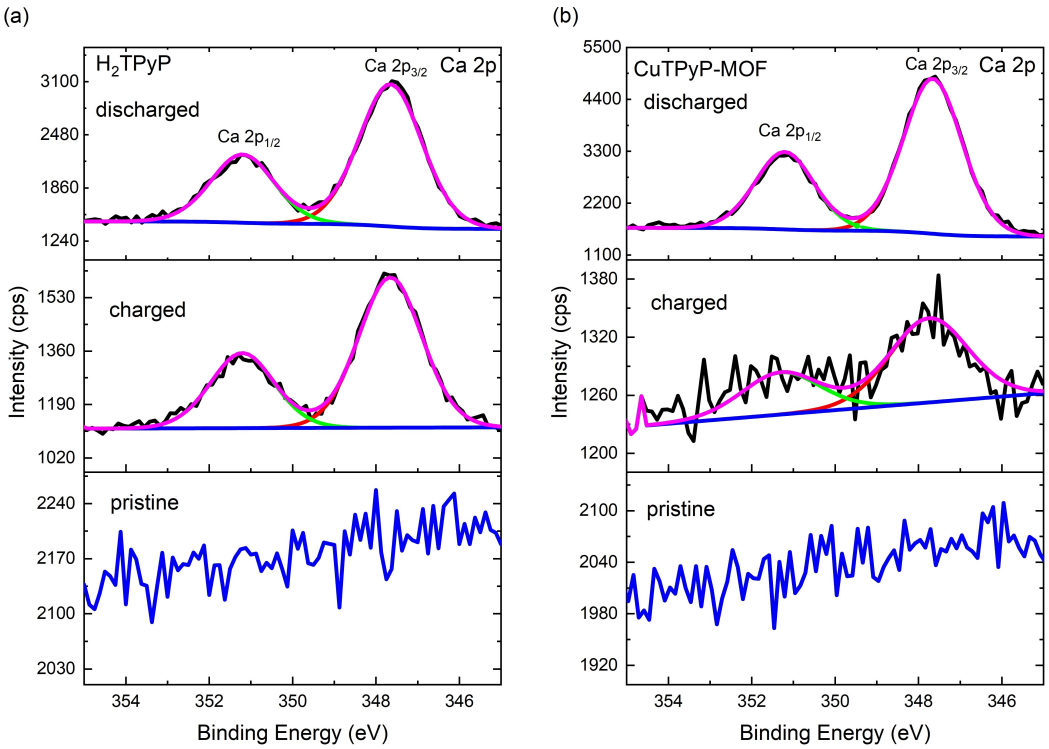

Figure 4. Ca 2p- XPS detail spectra of the pristine, charged (at 3.3 V) and discharged state (at 0.5 V) of a) H_2TPyP and b) CuTPyP–MOF.

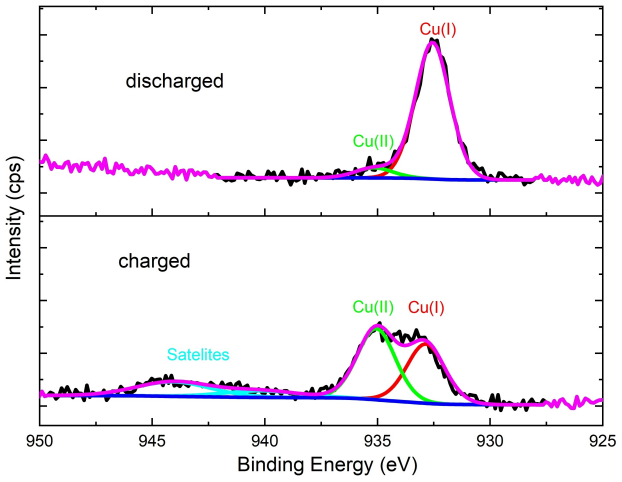

Figure 5. Cu $2p_{3/2}$-XPS detail spectra of CuTPyP–MOF electrodes in the charged (at 3.3 V) and discharged (at 0.5 V) state.

In the charged state, a rather equivalent mixture of both oxidation states was observed. This could be due to the earlier discussed existence of Cu(I) at the nodes of Cu–MOFs[36] and is therefore interlinked with a partial return to the default structure. Besides we speculate that a minor amount of copper ions might not be converted back to its initial state due to previously discussed interaction with calcium ions nudging them out of the porphyrin core.

The improvement from the copper redox reaction is evident when comparing the cycling performance and rate capability of CuTPyP–MOF and H_2TPyP (Figure 6a and b). Both compounds exhibited remarkable results, with the calcium cells cycling for up to 3000 cycles. However, CuTPyP–MOF delivered higher reversible capacity, reaching up to 115 mAh/g at a current density of 1 A/g. The CuTPyP–MOF revealed outstanding capacity retention of 78% after 3000 cycles, while H_2TPyP had a cycling stability of 72%. The first cycle was excluded from this consideration due to the earlier discussed irreversible calcium ion trapping, which made comparison difficult. It is also important to mention that for the cycling stability of both materials for the first 500 cycles an activation process occurs. Both porphyrins also demonstrated excellent rate capability (Figure 6b and c) while cycled at various current densities between 0.2 A/g and 2 A/g. Excellent capacity retention of 90 mAh/g at a high rate of 2 A/g highlights the immense potential of CuTPyP–MOF as high-power cathode in calcium batteries. Moreover, the materials were capable to recover their initially capacities when charged with lower currents again.

No plateaus were observed in the charge-discharge cycles of porphyrinic cells (Figures 6d, S23), indicating a fast redox reaction at porphyrin sites and pseudocapacitive behavior, that have been well documented in literature.[25a,29,41a] To further investigate this pseudocapacity and gain a more comprehensive understanding of the underlying processes in porphyrin–calcium cells, a detailed kinetic analysis of these materials was performed (Figure 7, according to Equation S1) in order to disentangle diffusion and surface-controlled processes. At lower scan rates, both charge storage mechanisms contribute significantly (roughly 50:50 ratio at 2 mV/s). At higher scan rates, the estimated surface contribution becomes dominant, implying effective non-faradaic charge storage. The altered

Research Article
doi.org/10.1002/batt.202300308
Chemistry Europe
European Chemical Societies Publishing

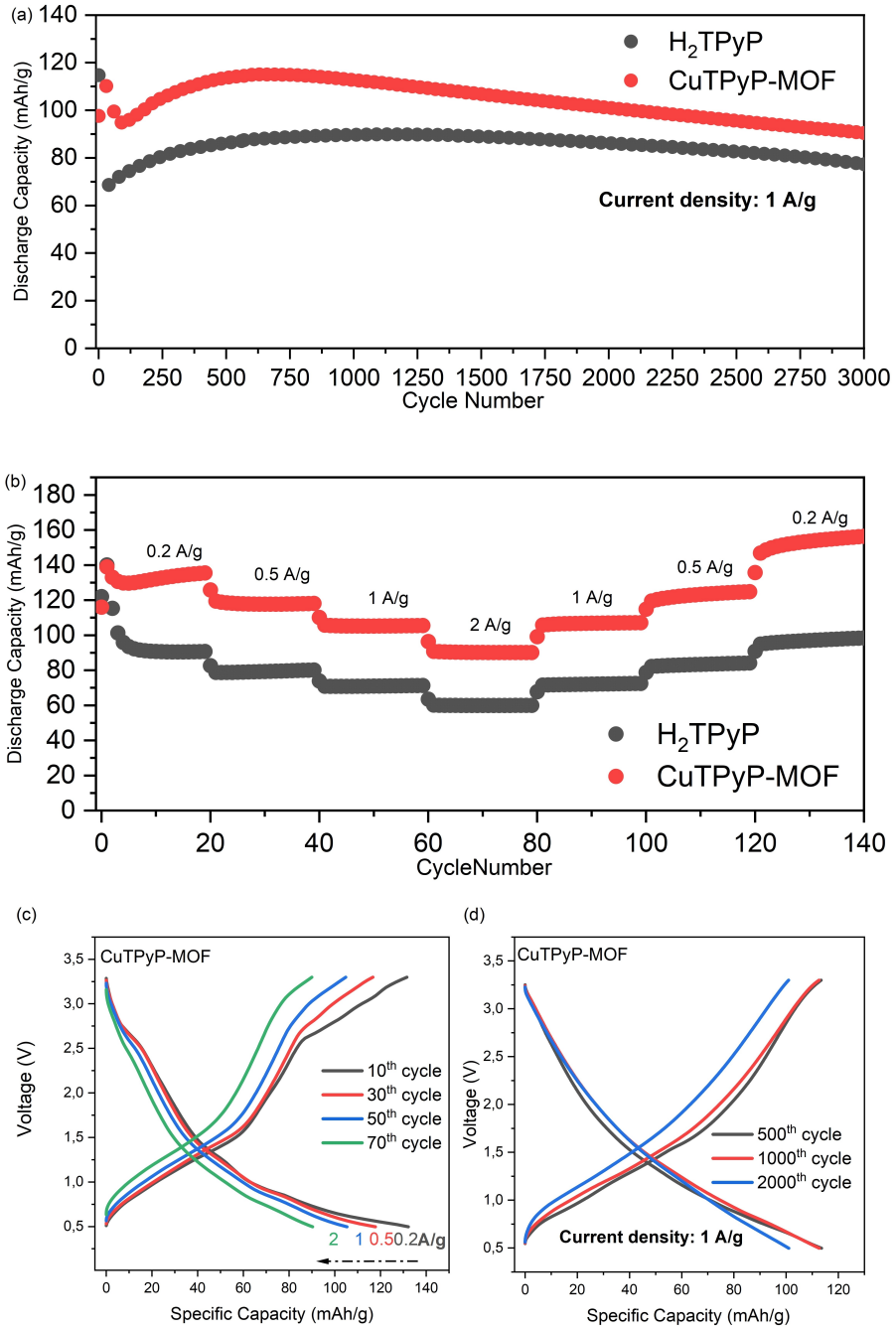

Figure 6. Comparison of CuTPyP–MOF with H_2TPyP with regard to a) cycling performance at a current density of 1 A/g and b) rate capability. Selected charge discharge profiles of CuTPyP–MOF c) at differing current densities and d) upon prolonged cycling at 1 A/g.

structure of CuTPyP–MOF, in comparison to H_2TPyP (Figure S24), results in a large contribution from diffusion-controlled reaction, indicating a more battery-like material character. This stands in contrast to previous studies, which showed dominant surface reactions upon the introduction of a copper ion.[25a,29,41a] Interestingly, the stronger faradaic character of CuTPyP–MOF does not influence the rate capability.

Conclusions

In conclusion, this study has demonstrated for the first time the potential of porphyrin materials as cathode materials in calcium batteries. Both porphyrin structures, H_2TPyP and CuTPyP–MOF, exhibited remarkable cycling stability up to 3000 cycles and proved to be effective hosts for calcium ions. Furthermore, the structures delivered high discharge capacity even at elevated current densities, making them attractive for high-power applications. *Ex-situ* studies were conducted to complement the understanding of the mechanism of porphyrin active materials

Research Article
doi.org/10.1002/batt.202300308
Chemistry Europe
European Chemical Societies Publishing

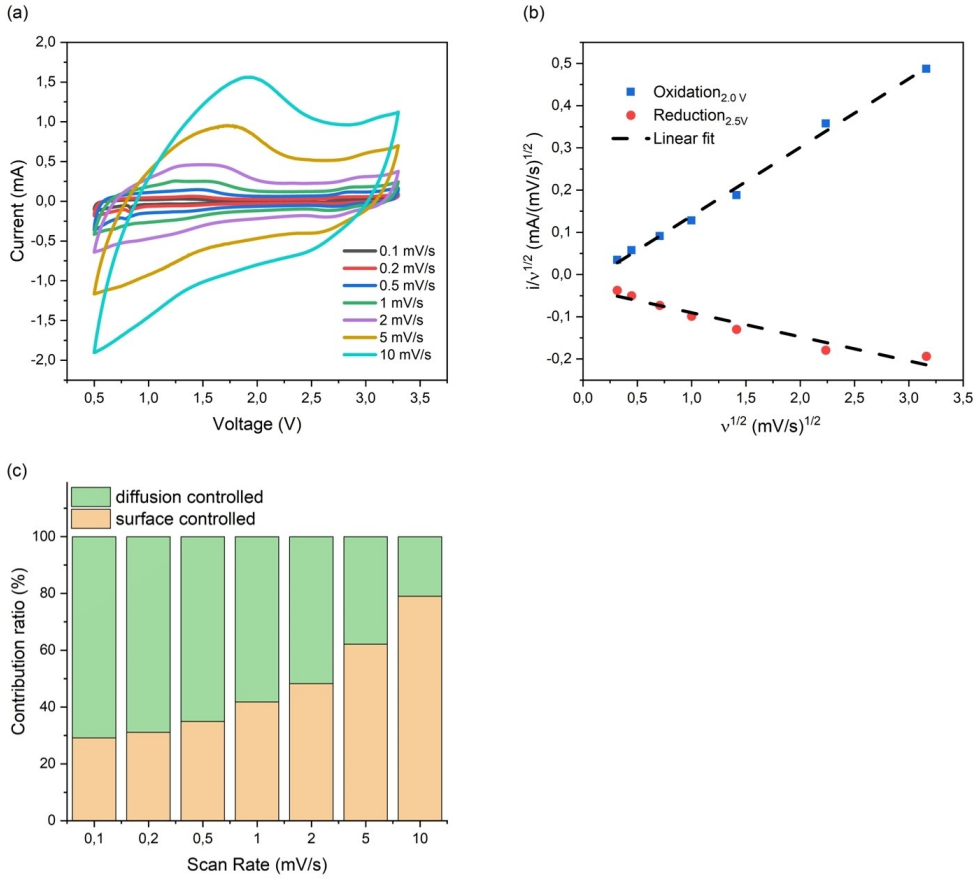

Figure 7. Kinetic analysis of CuTPyP–MOF: a) CV curves at different scanning rates (0.1–10 mV/s) and b) plot of $i_v/v^{1/2}$ vs. $v^{1/2}$. c) The corresponding calculated contribution ratio of diffusion- and surface-controlled charge storage at scan rates between 0.1–10 mV/s.

in calcium batteries. Electrochemical performance analysis revealed that the presence of copper in the structure strongly influenced the cycling performance through extra Cu(II)/Cu(I) redox reactions. The improvement was further elucidated, by kinetic analysis, which linked it to the pseudocapacitive nature of the material. Therefore, this study highlights the potential of (metal) porphyrins as cathode materials in calcium batteries and opens up new possibilities for sustainable energy storage systems.

Experimental Section

Materials. Metal-free 5,10,15,20-tetrapyridyl porphyrin (H_2TPyP) was obtained commercially (PorphyChem SAS, France) and was used without further purification. Conductive carbon (Ketjenblack EC600JD, AkzoNobel) and polyvinylidene fluoride (PVDF, Alfa Aesar) were dried in vacuum (1×10^{-3} mbar) for at least 12 h at 300 °C or 100 °C, respectively. Glass microfiber separators (Whatman, GF/C) were dried at 200 °C in vacuum for over 12 h. The synthesis and processing of both, the alloy anode and the electrolyte, are described elsewhere.[19]

Synthesis of 5,10,15,20-(tetra(4-pyridyl)porphinato)copper(II)-metal organic framework (CuTPyP–MOF). The free-base porphyrin (H_2TPyP) (1 g, 1.61 mmol) and $Cu(OAc)_2\cdot4H_2O$ (4 g, 20.04 mmol) were dissolved in 300 mL chloroform and 100 mL methanol. The reaction mixture was stirred at room temperature for 1 day. The solvent was removed under vacuum. The crude product was washed with water and methanol to remove the unreacted Cu-salt. The product, a red solid, was dried in vacuum.

UV-Vis ($CHCl_3$): 418, 543 nm; **FT-IR**: $\tilde{\nu}=1619$, 1603, 1422, 1347, 1222, 1073, 1000, 799, 679 cm^{-1}; **Elemental analysis**: C 49.89 %, H 3.88 %, N 10.24 % (calcd. for $C_{56}H_{48}Cu_5N_8O_{16}$: C 47.81 %, H 3.44 %, N 7.97 %).

Computational details. Quantum chemical calculations were performed on the bwForCluster JUSTUS 2 at the University of Ulm, using release C.01 of the Gaussian16 program package and also using DFT calculations using B3LYP functional along with def2-TZVP basis set in the implicit solvation model Conductor-like Polarizable Continuum Model (CPCM) with chloroform as a solvent. The converged structures were found to be local energetic minima, as established by frequency calculations. To explain the origin of the redshift of the Q-band in UV spectra after insertion of the Cu(II), we performed time-dependent DFT (TD-DFT) calculations to find the electronic transitions and relationships with occupied and unoccupied molecular orbitals.

Computed structures. Molecular geometry and electronic properties were computed for the free base 5,10,15,20-tetrapyridyl porphyrin (H_2TPyP), and its Cu(II) complex CuTPyP. Neutral CuTPyP has one unpaired electron and was therefore computed as doublet. The anionic complex $[CuTPyP]^{-1}$ was computed in the singlet state. For the anion M06-2X/TZVP was used and the pseudo potential MDF10 for Cu; solvent model: PCM with THF as solvent.

Research Article
doi.org/10.1002/batt.202300308

Cathode preparation. For the electrode slurry, tetrapyridylporphyrins, H_2TPyP and CuTPyP–MOF, were mixed with Ketjenblack and PVDF with a respective ratio of 0.6:0.3:0.1 in N-methyl-2-pyrrolidone (NMP). For mixing the substances, a planetary centrifugal mixer (ThinkyARE-250) was utilized at 2000 rpm for 20 minutes. The slurry was applied on a graphite-based gas diffusion layer (GDL 29AA, Ion Power, Germany) and the electrode was pre-dried overnight. The electrode was cut into discs (11.8 mm diameter) and dried in vacuum (1×10^{-3} mbar) at 80 °C for 12 h. The mass loading of electrodes was ~2 mg/cm^2. The electrode discs were transferred and stored in an Argon-filled glove box.

Electrochemical cell tests. Electrochemical cell tests were performed on a Biologic BCS 805 testing unit with an applied voltage window between 0.5 V and 3.3 V. For testing, CR2032 coin cells were built with a $CaSn_3$-alloy as anode and 0.3 M $Ca[B(hfip)_4]_2$ in DME as electrolyte. Cyclic voltammetry measurements were recorded with differing scan rates between 0.1 to 10 mV/s, whereas galvanostatic cycling was performed with constant currents of 0.1 A/g and 1 A/g. Only exceptions were the rate capability experiments which were tested with currents between 0.2 A/g to 2 A/g.

Structural and chemical characterization. The XPS measurements were carried out with a PHI 5800 MultiTechnique ESCA System (Physical Electronics) using monochromatic Al–Kα (1486.6 eV) radiation, a detection angle of 45°, and pass energies at the analyzer of 93.9 and 29.35 eV for survey and detail spectra, respectively. The samples were neutralized with electrons from a flood gun (current 3 μA) to compensate for charging effects at the surface. For binding energy calibration, the main C(1 s) peak was set to 284.8 eV. Peak fitting was carried out with Casa XPS software with Shirley-type backgrounds and Gaussian-Lorentzian peak profiles. SEM imaging was conducted in a Zeiss Leo Gemini 1530 System. EDX measurements were conducted on an Apreo 2 SEM from Thermo Fisher Scientific, the Everhart Thornley Detector was operated in the secondary electron mode. The EDX was carried out with a voltage of 20 kV while the SEM imaging was done at an operating voltage of 5 kV. EDX spectra were collected for 60 s and elemental mapping was done for 300 s. X-ray powder diffraction (XRD) were recorded using STOE STADI P Diffractometer with Debye Scherer geometry using Mo–Kα-1 ($\lambda=0.7093$ Å) and Cu–Kα-1 radiation ($\lambda=1.5406$ Å). IR spectra were recorded with a Nicolet iS50 FTIR spectrometer. Measurements were carried out in a range of 400–4000 cm^{-1}. The elemental analysis was carried out in CHNS-mode using a Vario micro cube. UV-VIS spectra were collected on a Varian Cary 5000 UV-VIS/NIR spectrophotometer in chloroform.

Supporting Information

Additional references cited within the Supporting Information.[33a,44]

Acknowledgements

This work contributes to the research performed at CELEST (Center for Electrochemical Energy Storage Ulm-Karlsruhe) and was funded by the German Research Foundation (DFG) under Project ID 390874152 (POLiS Cluster of Excellence, EXC 2154). Open Access funding enabled and organized by Projekt DEAL.

Conflict of Interests

The authors declare no conflicts of interest.

Data Availability Statement

The data that support the findings of this study are available from the corresponding author upon reasonable request.

Keywords: calcium batteries · porphyrin complex · high current density · metal-organic framework · alloy anode

[1] a) D. Larcher, J.-M. Tarascon, *Nat. Chem.* **2015**, *7*, 19; b) M. Wei, C. A. McMillan, S. de la Rue du Can, *Curr. Sustainable/Renewable Energy Rep.* **2019**, *6*, 140; c) A. G. Boulanger, A. C. Chu, S. Maxx, D. L. Waltz, *Proc. IEEE* **2011**, *99*, 1116.
[2] a) Y. Nishi, *J. Power Sources* **2001**, *100*, 101; b) T. Kim, W. Song, D.-Y. Son, L. K. Ono, Y. Qi, *J. Mater. Chem. A* **2019**, *7*, 2942; c) J. B. Goodenough, K.-S. Park, *J. Am. Chem. Soc.* **2013**, *135*, 1167; d) T. Placke, R. Kloepsch, S. Dühnen, M. Winter, *J. Solid State Electrochem.* **2017**, *21*, 1939; e) M. Fichtner, *Batteries & Supercaps* **2022**, *5*, e202100224; f) N. Nitta, F. Wu, J. T. Lee, G. Yushin, *Mater. Today* **2015**, *18*, 252.
[3] a) M. A. Hannan, M. S. H. Lipu, A. Hussain, A. Mohamed, *Renewable Sustainable Energy Rev.* **2017**, *78*, 834; b) J. Jaguemont, L. Boulon, Y. Dubé, *Appl. Energy* **2016**, *164*, 99; c) J. W. Choi, D. Aurbach, *Nat. Rev. Mater.* **2016**, *1*, 16013; d) H. Kim, G. Jeong, Y.-U. Kim, J.-H. Kim, C.-M. Park, H.-J. Sohn, *Chem. Soc. Rev.* **2013**, *42*, 9011.
[4] H. Vikström, S. Davidsson, M. Höök, *Appl. Energy* **2013**, *110*, 252.
[5] a) L. Stievano, I. de Meatza, J. Bitenc, C. Cavallo, S. Brutti, M. A. Navarra, *J. Power Sources* **2021**, *482*, 228875; b) M. Walter, M. V. Kovalenko, K. V. Kravchyk, *New J. Chem.* **2020**, *44*, 1677.
[6] D. Monti, A. Ponrouch, R. B. Araujo, F. Barde, P. Johansson, M. R. Palacín, *Front. Chem.* **2019**, *7*, 79.
[7] A. Ponrouch, J. Bitenc, R. Dominko, N. Lindahl, P. Johansson, M. R. Palacin, *Energy Storage Mater.* **2019**, *20*, 253.
[8] A. Ponrouch, M. R. Palacín, *Phil. Trans. R. Soc. A* **2019**, *377*, 20180297.
[9] a) R. Mohtadi, O. Tutusaus, T. S. Arthur, Z. Zhao-Karger, M. Fichtner, *Joule* **2021**, *5*, 581; b) R. J. Gummow, G. Vamvounis, M. B. Kannan, Y. He, *Adv. Mater.* **2018**, *30*, 1801702.
[10] M. E. Arroyo-de Dompablo, A. Ponrouch, P. Johansson, M. R. Palacín, *Chem. Rev.* **2020**, *120*, 6331.
[11] K. H. Wedepohl, *Geochim. Cosmochim. Acta* **1995**, *59*, 1217.
[12] D. S. Jacks, M. Stuermer, *Energy Econ.* **2020**, *85*, 104035.
[13] G. Rayner-Canham, T. Overton, *Descriptive Inorganic Chemistry*, Macmillan, **2009**.
[14] a) R. D. Shannon, *Acta Crystallogr. Sect. A* **1976**, *32*, 751; b) R. T. Shannon, C. T. Prewitt, *Acta Crystallogr. Sect. B* **1969**, *25*, 925.
[15] a) S. Gheytani, Y. Liang, F. Wu, Y. Jing, H. Dong, K. K. Rao, X. Chi, F. Fang, Y. Yao, *Adv. Sci.* **2017**, *4*, 1700465; b) D. S. Tchitchekova, A. Ponrouch, R. Verrelli, T. Broux, C. Frontera, A. Sorrentino, F. Bardé, N. Biskup, M. E. Arroyo-de Dompablo, M. R. Palacín, *Chem. Mater.* **2018**, *30*, 847; c) M. Liu, Z. Rong, R. Malik, P. Canepa, A. Jain, G. Ceder, K. A. Persson, *Energy Environ. Sci.* **2015**, *8*, 964.
[16] B. Ji, H. He, W. Yao, Y. Tang, *Adv. Mater.* **2021**, *33*, 2005501.
[17] a) A. Ponrouch, C. Frontera, F. Bardé, M. R. Palacín, *Nat. Mater.* **2016**, *15*, 169; b) H. Song, J. Su, C. Wang, *Adv. Mater.* **2021**, *33*, 2006141.
[18] D. Aurbach, R. Skaletsky, Y. Gofer, *J. Electrochem. Soc.* **1991**, *138*, 3536.
[19] a) Z. Zhao-Karger, Y. Xiu, Z. Li, A. Reupert, T. Smok, M. Fichtner, *Nat. Commun.* **2022**, *13*, 3849; b) Z. Li, O. Fuhr, M. Fichtner, Z. Zhao-Karger, *Energy Environ. Sci.* **2019**, *12*, 3496.
[20] X. Xu, M. Duan, Y. Yue, Q. Li, X. Zhang, L. Wu, P. Wu, B. Song, L. Mai, *ACS Energy Lett.* **2019**, *4*, 1328.
[21] a) M. D. Levi, E. Lancry, H. Gizbar, Z. Lu, E. Levi, Y. Gofer, D. Aurbach, *J. Electrochem. Soc.* **2004**, *151*, A1044; b) E. Levi, M. D. Levi, O. Chasid, D. Aurbach, *J. Electroceram.* **2009**, *22*, 13; c) Z. Rong, R. Malik, P. Canepa, G. Sai Gautam, M. Liu, A. Jain, K. Persson, G. Ceder, *Chem. Mater.* **2015**, *27*, 6016; d) P. Canepa, G. Sai Gautam, D. C. Hannah, R. Malik, M. Liu, K. G. Gallagher, K. A. Persson, G. Ceder, *Chem. Rev.* **2017**, *117*, 4287.

[22] a) K. Qin, J. Huang, K. Holguin, C. Luo, *Energy Environ. Sci.* **2020**, *13*, 3950; b) Y. Chen, K. Fan, Y. Gao, C. Wang, *Adv. Mater.* **2022**, *34*, 2200662.
[23] a) P. Poizot, J. Gaubicher, S. Renault, L. Dubois, Y. Liang, Y. Yao, *Chem. Rev.* **2020**, *120*, 6490; b) H. Nishide, *Green Chem.* **2022**, *24*, 4650.
[24] a) X. Xiao, L. Zou, H. Pang, Q. Xu, *Chem. Soc. Rev.* **2020**, *49*, 301; b) C. Ding, C. Li, H. Tian, Y. Tong, W. Huang, Q. Zhang, *Batteries & Supercaps* **2022**, *5*, e202200160; c) J. Xie, Z. Wang, Z. J. Xu, Q. Zhang, *Adv. Energy Mater.* **2018**, *8*, 1703509.
[25] a) T. Smok, E. Abouzari-Lotf, S. Frentzen, T. Diemant, M. Fichtner, *Batteries & Supercaps* **2023**, *n/a*, e202300026; b) P. Gao, Z. Chen, Z. Zhao-Karger, J. E. Mueller, C. Jung, S. Klyatskaya, T. Diemant, O. Fuhr, T. Jacob, R. J. Behm, *Angew. Chem.* **2017**, *129*, 10477.
[26] X. Chen, X. Feng, B. Ren, L. Jiang, H. Shu, X. Yang, Z. Chen, X. Sun, E. Liu, P. Gao, *Nano-Micro Lett.* **2021**, *13*, 1.
[27] S. Lv, J. Yuan, Z. Chen, P. Gao, H. Shu, X. Yang, E. Liu, S. Tan, M. Ruben, Z. Zhao-Karger, M. Fichtner, *ChemSusChem* **2020**, *13*, 2286.
[28] X. Han, S. Li, W.-L. Song, N. Chen, H. Chen, S. Huang, S. Jiao, *Adv. Energy Mater.* **2021**, *11*, 2101446.
[29] E. Abouzari-Lotf, R. Azmi, Z. Li, S. Shakouri, Z. Chen, Z. Zhao-Karger, S. Klyatskaya, J. Maibach, M. Ruben, M. Fichtner, *ChemSusChem* **2021**, *14*, 1840.
[30] Z. Zhao-Karger, P. Gao, T. Ebert, S. Klyatskaya, Z. Chen, M. Ruben, M. Fichtner, *Adv. Mater.* **2019**, *31*, 1806599.
[31] a) J. Heiska, M. Nisula, M. Karppinen, *J. Mater. Chem. A* **2019**, *7*, 18735; b) J. Y. Shin, T. Yamada, H. Yoshikawa, K. Awaga, H. Shinokubo, *Angew. Chem.* **2014**, *126*, 3160; c) Z. Song, H. Zhou, *Energy Environ. Sci.* **2013**, *6*, 2280.
[32] a) F. He, Y. Zhou, X. Chen, T. Wang, Y. Zeng, J. Zhang, Z. Chen, W. Liu, P. Gao, *Chem. Commun.* **2023**, *59*, 2787; b) F.-H. Wang, Z.-Y. Liu, S. Yang, L. Shi, D.-Z. Lin, H.-Y. Liu, G.-Q. Yuan, *Synth. Commun.* **2021**, *51*, 2053.
[33] a) T. Ohmura, N. Setoyama, Y. Mukae, A. Usuki, S. Senda, T. Matsumoto, K. Tatsumi, *CrystEngComm* **2017**, *19*, 5173; b) T. Ohmura, A. Usuki, K. Fukumori, T. Ohta, M. Ito, K. Tatsumi, *Inorg. Chem.* **2006**, *45*, 7988.
[34] A. Sengupta, S. Datta, C. Su, T. S. Herng, J. Ding, J. J. Vittal, K. P. Loh, *ACS Appl. Mater. Interfaces* **2016**, *8*, 16154.
[35] G. Socrates, *Infrared and Raman characteristic group frequencies: tables and charts*, John Wiley & Sons, **2004**.
[36] A. S. Duke, E. A. Dolgopolova, R. P. Galhenage, S. C. Ammal, A. Heyden, M. D. Smith, D. A. Chen, N. B. Shustova, *J. Phys. Chem. C* **2015**, *119*, 27457.
[37] P. St. Petkov, G. N. Vayssilov, J. Liu, O. Shekhah, Y. Wang, C. Wöll, T. Heine, *ChemPhysChem* **2012**, *13*, 2025.
[38] L. Alaerts, E. Séguin, H. Poelman, F. Thibault-Starzyk, P. A. Jacobs, D. E. De Vos, *Chem. Eur. J.* **2006**, *12*, 7353.
[39] a) J. Martí-Rujas, *Dalton Trans.* **2020**, *49*, 13897; b) F. Gandara, T. D. Bennett, *IUCrJ* **2014**, *1*, 563.
[40] a) L. Bugnon, C. J. H. Morton, P. Novak, J. Vetter, P. Nesvadba, *Chem. Mater.* **2007**, *19*, 2910; b) J. J. Shea, C. Luo, *ACS Appl. Mater. Interfaces* **2020**, *12*, 5361.
[41] a) S. Shakouri, E. Abouzari-Lotf, J. Chen, T. Diemant, S. Klyatskaya, F. D. Pammer, A. Mizuno, M. Fichtner, M. Ruben, *ChemSusChem* **2023**, 16, e202202090; b) X. Feng, X. Chen, B. Ren, X. Wu, X. Huang, R. Ding, X. Sun, S. Tan, E. Liu, P. Gao, *ACS Appl. Mater. Interfaces* **2021**, *13*, 7178.
[42] Y. Zhou, X. Huang, X. Chen, F. He, D. Chen, X. Sun, S. Tan, P. Gao, *ACS Appl. Mater. Interfaces* **2022**, *14*, 40862.
[43] M.-S. Liao, S. Scheiner, *J. Chem. Phys.* **2002**, *117*, 205.
[44] a) W. Mäntele, E. Deniz, *Spectrochim. Acta Part A* **2017**, *173*, 965; b) J. Wang, J. Polleux, J. Lim, B. Dunn, *J. Phys. Chem. C* **2007**, *111*, 14925.

Manuscript received: August 17, 2023
Revised manuscript received: September 10, 2023
Accepted manuscript online: September 11, 2023
Version of record online: September 28, 2023